

## Fast magnetoacoustic waves in a fan structure above the coronal magnetic null point

H. Mészárosová<sup>1,2</sup> · J. Dudík<sup>2,3</sup> ·  
M. Karlický<sup>2</sup> · F. R. H. Madsen<sup>1</sup> ·  
H. S. Sawant<sup>1</sup> ·

Received ; accepted

© Springer ●●●

**Abstract** We analyze the 26 November 2005 solar radio event observed interferometrically at frequencies of 244 and 611 MHz by the *Giant Metrewave Radio Telescope* (GMRT) in Pune, India. These observations are used to make interferometric maps of the event at both frequencies with the time cadence of 1 s from 06:50 to 07:12 UT. These maps reveal several radio sources. The light curves of these sources show that only two sources at 244 MHz and 611 MHz are well correlated in time. The EUV flare is more localized with flare loops located rather away from the radio sources. Using the SoHO/MDI observations and potential magnetic field extrapolation we demonstrate that both the correlated sources are located in the fan structure of magnetic field lines starting from a coronal magnetic null point. Wavelet analysis of the light curves of the radio sources detects tadpoles with periods in the range  $P = 10\text{--}83$  s. These wavelet tadpoles indicate the presence of fast magnetoacoustic waves that propagate in the fan structure of the coronal magnetic null point. We estimate the plasma parameters in the studied radio sources and find them consistent with the presented scenario involving the coronal magnetic null point.

**Keywords:** Sun: corona – Sun: flares – Sun: radio radiation – Sun: oscillations – Methods: data analysis

---

<sup>1</sup>National Space Research Institute (INPE), Ave. dos Astronautas 1758, 1221-0000 São José dos Campos, SP, Brazil, (e-mail: frhmadsen@gmail.com, sawant@das.inpe.br)

<sup>2</sup>Astronomical Institute of the Academy of Sciences, CZ-25165 Ondřejov, Czech Republic, (e-mail: hana@asu.cas.cz, karlicky@asu.cas.cz)

<sup>3</sup>Dept. of Astronomy, Physics of the Earth and Meteorology, Faculty of Mathematics, Physics and Informatics, Comenius University, SK-842 48 Bratislava, Slovak Republic, (e-mail: dudik@fmph.uniba.sk)

## 1. Introduction

It is commonly believed that the primary energy release regions in solar flares are located in the low corona (Aschwanden, 2005). Radio spectral and imaging observations in the decimetric and metric wavelength ranges in combination with magnetic field extrapolations are considered to be very promising tools for a study of these processes. Unfortunately, imaging observations of solar flares in the decimetric range are very rare. In the metric range, such observations are commonly done by the Nançay radioheliograph (Kerdraon and Delouis, 1997).

To successfully combine radio observations and magnetic extrapolations, the radio observations have to include sufficiently precise positional information. Such a combination was done *e.g.* by Trottet *et al.* (2006), where a detailed analysis of radio spectral and imaging observations in the 10–4500 MHz range was presented for the 5 November 1998 flare. Subramanian *et al.* (2007) have studied a post-flare source imaged at 1060 MHz to calculate the power budget for the efficiency of the plasma emission mechanism in a post-flare decimetric continuum source. Aurass, Rausche, and Mann (2007) have analyzed the topology of the potential coronal magnetic field near the source site of the meter-decimeter radio continuum to find that this radio source occurs near the contact of three separatrixes between magnetic flux cells. Aurass *et al.* (2011) have examined meter-decimeter dynamic radio spectra and imaging with longitudinal magnetic field magnetograms to describe meter-wave sources. Chen *et al.* (2011) have used an interferometric dm-radio observation and nonlinear force-free field extrapolation to explore the zebra pattern source in relation to the magnetic field configuration. Zuccarello *et al.* (2011) investigated the morphological and magnetic evolution of an active region before and during an X3.8 long duration event. They found that coronal magnetic null points played an important role in this flare.

A comprehensive review of magnetic fields and magnetic reconnection theory as well as observational findings was provided by Aschwanden (2005). The topological methods for the analysis of magnetic fields were reviewed in Longcope (2005) and the 3D null point reconnection regimes in Priest and Pontin (2009). McLaughlin, Hood, and De Moortel (2011) have presented a review of the theoretical studies of the MHD waves in the vicinity of the magnetic null points. Furthermore, Afanasyev and Uralov (2012) have studied analytically the propagation of a fast-mode magnetohydrodynamic wave near a 2D magnetic null point. Using the nonlinear geometrical acoustic method they have found complex behavior of these waves in the vicinity of this point. In spite of the wealth of theoretical work presented in these papers, the authors concluded that there is still no clear observational evidence for the presence of MHD waves near null points of the magnetic field. We note that this is also in spite the fact that MHD waves are commonly observed in the solar corona (De Moortel, Ireland, and Walsh, 2000; Kliem *et al.*, 2002; Harrison, Hood, and Pike, 2002; Tomczyk *et al.*, 2007; Ofman and Wang, 2008; De Moortel, 2009; Marsh, Walsh, and Plunkett, 2009; Marsh, De Moortel, and Walsh, 2011).

Since both the standing and propagating magnetoacoustic waves modulate the plasma density and the magnetic field in the radio source (Aschwanden, 2005), some modulation of the radio emission by both these waves can be expected.

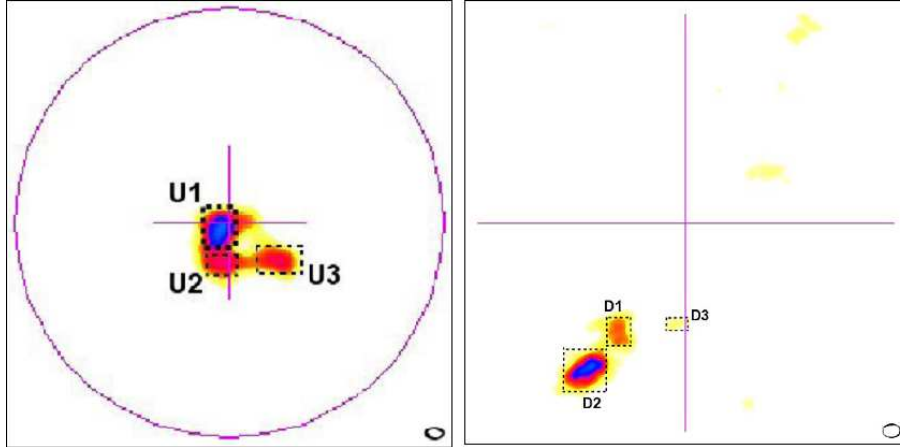


**Figure 1.** Solar maps with main sources associated with the 26 November 2005 radio event observed at 7:01:30 UT by the GMRT instrument. Regions U1–U3 and D1–D3 were identified as the main radio sources at 244 and 611 MHz, respectively. The magenta circle in the left panel has the diameter of 32 arc min and indicates an approximate position and size of the visible solar disk. Disk centers are shown by a cross. The cross has dimensions of  $400''$  in both directions to indicate the scale in the maps. Synthesized beam dimensions giving the error in GMRT positions are represented by the small ovals shown on the bottom right corners.

Roberts, Edwin, and Benz (1983, 1984) studied impulsively generated fast magnetoacoustic waves trapped in a structure with enhanced density (*e.g.* loop). They showed that these propagating waves exhibit both periodic and quasi-periodic phases. Nakariakov *et al.* (2004) numerically modelled impulsively generated fast magnetoacoustic wave trains and showed that the quasi-periodicity is a consequence of the dispersion of the guided modes. Using wavelet analysis, these authors found that typical wavelet spectrum of such fast magnetoacoustic wave trains is a tadpole consisting of a broadband head preceded by a narrowband tail.

The tadpoles as characteristic wavelet signatures of fast magnetoacoustic wave trains were observed in solar eclipse data (Katsiyannis *et al.*, 2003) as well as in radio spectra of decimetric gyrosynchrotron emission (Mészárosová *et al.*, 2009a), and also in decimetric plasma emission (Mészárosová *et al.*, 2009b). While the tadpoles in the gyrosynchrotron emission was detected simultaneously at all radio frequencies, the tadpoles in the plasma emission drifted towards low frequencies. This type of “drifting tadpoles” was studied in details in Mészárosová, Karlický, and Rybák (2011) in the radio dynamical spectrum with fibers.

The observed parameters of fast magnetoacoustic waves reflect properties of the plasma in the waveguides where these waves are propagating. Therefore, one could use observed waves and their wavelet tadpoles as a potentially useful diagnostic tool (Jelínek and Karlický, 2009; Jelínek and Karlický, 2010) for determining physical conditions in these waveguides, (*e.g.* loops or current sheets). Karlický, Jelínek, and Mészárosová (2011) compared parameters of wavelet tadpoles detected in the radio dynamical spectra with narrowband spikes to those

**Table 1.** Time evolution of the individual GMRT sources.

Source	Start time [UT]	Time of max [UT]	End time [UT]
U1	6:58:04	7:01:30	7:04:03
U2	6:57:59	7:01:30	
U3	6:58:20	7:06:45	
D1	6:58:05	7:03:52	7:05:11
D2	6:58:54	6:59:33	7:04:00
D3	6:58:13	6:58:43	7:01:59

computed in the model with the Harris current sheet. Based on this comparison the authors proposed that the spikes are generated by driven coalescence and fragmentation processes in turbulent reconnection outflows. We note here that, in general, flare current sheets can be formed not only near magnetic null points, but also *e.g.* between interacting magnetic loops. Jelínek and Karlický (2012) numerically studied impulsively generated magnetoacoustic waves for the Harris current sheet and a density slab. In both cases they find that wave trains were generated and propagated in a similar way for similar geometrical and plasma parameters.

In this paper, we analyze a rare decimetric imaging observation of the 26 November 2005 solar flare made by the *Giant Metrewave Radio Telescope* (GMRT). Combing the results of this analysis with the magnetic field extrapolation (Section 3), we present a scenario of this radio event. For the first time, we detected the magnetoacoustic waves in the radio sources (Section 4) located in the fan of magnetic field lines connected with a coronal null point. The basic plasma parameters in the radio sources are estimated and the results are discussed (Section 5).

## 2. Observations and data analysis

The B8.9 solar flare occurred on 26 November 2005 in the active regions NOAA AR 10824 and 10825 located near the disk center. The flare lasted from approximately 06:31 to 07:49 UT with the GOES maximum at 07:05 UT.

The radio counterpart of this flare was a 22 minutes long radio event lasting from the 06:50 to 07:12 UT recorded by the *Giant Metrewave Radio Telescope* (GMRT) in Pune, India. The *Michelson Doppler Imager* (MDI, Scherrer *et al.* 1995) onboard the SoHO spacecraft (Domingo, Fleck, and Poland, 1995) performed routine full-disk observations with a 96 minute cadence. The magnetogram nearest to the radio event was observed at 06:24 UT. The EUV counterparts of this flare were observed by the *Extreme Ultraviolet Imaging Telescope* (Delaboudinière *et al.*, 1995) onboard the SoHO spacecraft.

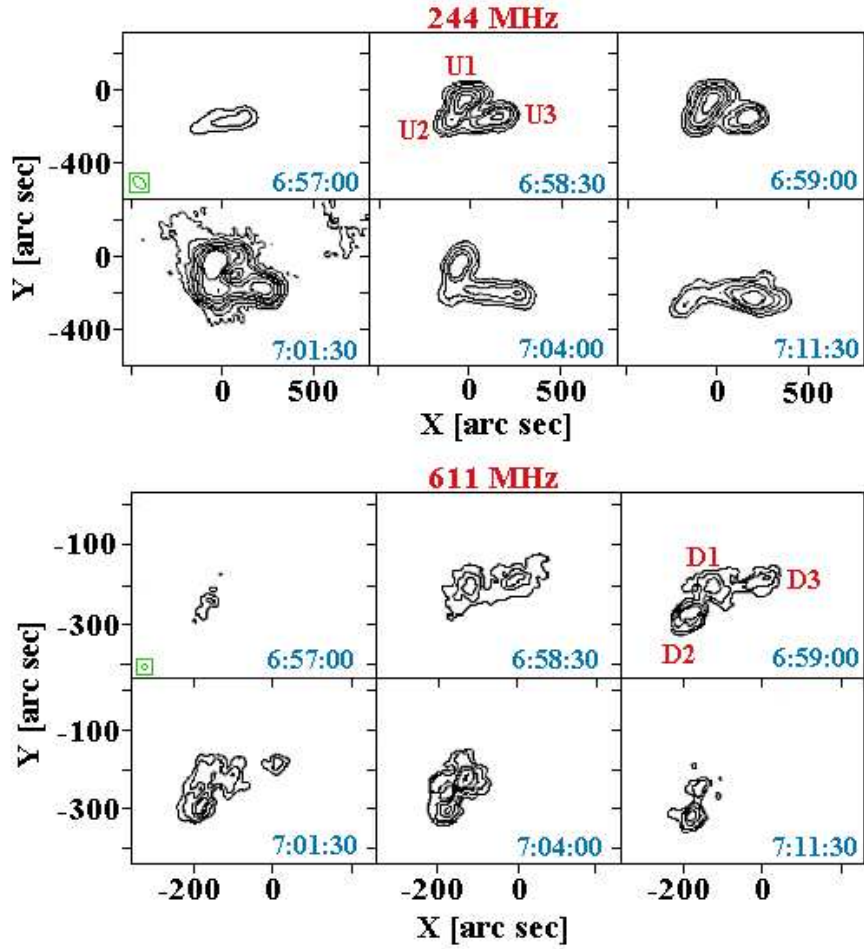


**Figure 2.** Selected contour maps showing the time evolution of the emission sources at 244 MHz (upper panel) and 611 MHz (bottom panel). The times (UT) are in blue. Synthesized beam dimensions representing the error in GMRT positions are shown as small green circles on the bottom left corners of maps at 6:57 UT. Upper panel: Positions of the sources U1–U3 (in red) are indicated on the map at 6:58:30 UT. Bottom panel: Positions of the sources D1–D3 (in red) are indicated on the map at 6:59 UT.

### 2.1. GMRT observations and data analysis

On 26 November 2005, the GMRT observed the Sun at two frequencies, 244 and 611 MHz. The GMRT instrument (Swarup *et al.*, 1991; Ananthakrishnan and Rao, 2002; Mercier *et al.*, 2006) is a radio interferometer consisting of 30 fully steerable individual radio telescopes. Each telescope has a parabolic antenna with a diameter of 45 m and 16 of these individual antennas are arranged in an Y shape array with each arm having length of 14 km from the array centre. The remaining 14 telescopes are located in the central area of 1 km<sup>2</sup>. The interferometer operates at wavelengths longer than 21 cm, with six frequency bands centered on the 38,

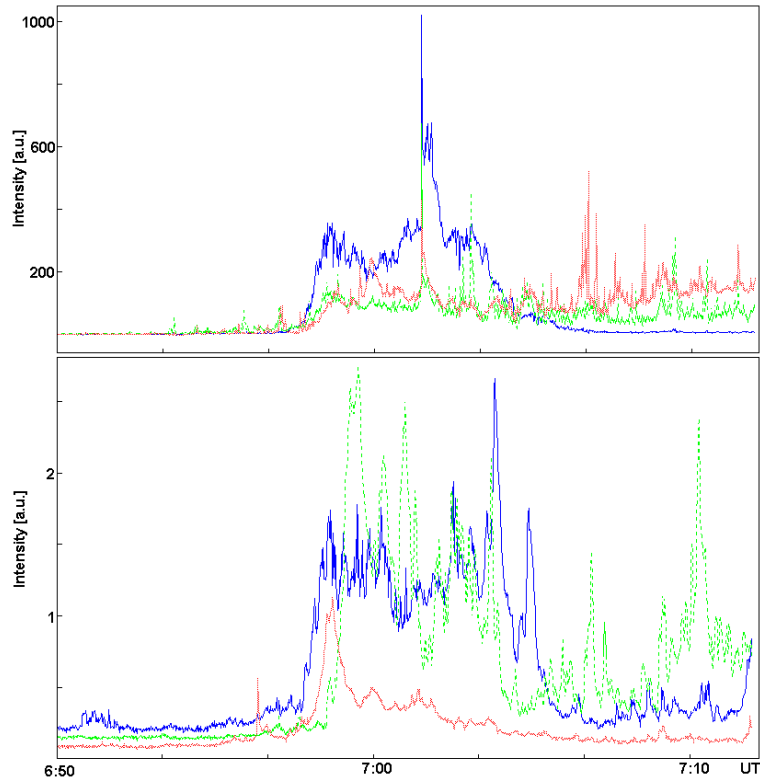


**Figure 3.** Light curves of the 26 November 2005 radio event obtained from the GMRT maps. Upper panel: Radio fluxes at 244 MHz corresponding to the sources U1 (blue), U2 (dashed green) and U3 (dotted red). Bottom panel: Radio fluxes at 611 MHz corresponding to the sources D1 (blue), D2 (dashed green) and D3 (dotted red).

153, 233, 327, 610, and 1420 MHz frequencies. The maximum resolution depends on the configuration, and varies between 2 and 60 arc secs.

The observed interferometric data at 244 and 611 MHz were Fourier transformed to generate a series of 1320 snapshot images of the Sun at 1 second time-cadence, from 06:50 to 07:12 UT. The images were cleaned using the algorithm developed by Schwab (1984) and rotated to correct for the solar North. The synthesized beam dimensions giving the GMRT positional error are  $77.7 \times 50.8$  and  $17.7 \times 13.4$  arc sec at 244 and 611 MHz, respectively.

An example of the observations showing the main radio sources is shown in Figure 1. On this figure, six sources can be identified, three for each frequency. At the frequency of 244 MHz, the sources are outlined in the left panel and denoted as U1, U2, and U3. The main sources at the frequency 611 MHz are shown in the right panel of Figure 1 and labelled as D1, D2, and D3. The evolution of these sources during the radio event is shown in Figure 2. Positions of the individual radio sources U1–U3 and D1–D3 are shown in red. Notable is the merging of

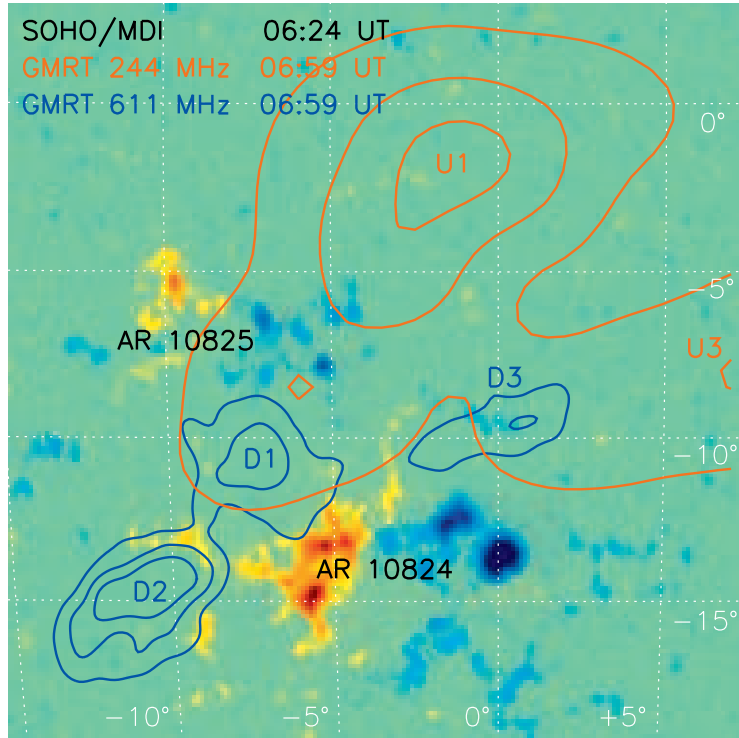


**Figure 4.** Superposition of the radio sources at 244 MHz (orange contours) and 611 MHz (blue contours) observed at 06:59 UT on top of the photospheric magnetic map obtained with the SoHO/MDI at 6:24 UT. Individual radio sources are labelled. The MDI magnetogram is saturated to  $\pm 10^3$  G. Heliographic coordinates are shown for orientation. Solar North is up.

the sources U1 and U2 at around 6:59 UT. The source U3 remains far from the others (U1 and U2).

We constructed light curves of the individual radio sources by enclosing these sources in rectangular regions on the GMRT maps. The light curves are shown in Figure 3. The radio fluxes at 244 MHz corresponding to the sources U1, U2, and U3 are shown in the upper panel as the blue, dashed green and dotted red lines, respectively. The radio fluxes at 611 MHz frequency corresponding to the sources D1 (blue), D2 (dashed green) and D3 (dotted red) are present in the bottom panel. The calibration of the individual fluxes is relative only and is expressed in arbitrary units (a.u.).

Analysis of these time series of radio fluxes shows different time evolution profiles for the different radio sources. The sources U1, D1, and D3 show about 5 minutes durations with a well defined main peak. On the other hand, the sources U2, U3, and D2 show profiles with a gradual rise and several peaks on top of a roughly constant background. The temporal properties of these sources are presented in Table 1. The start and end times of each source were determined as the times when the fluxes were above or below half the average flux of the whole burst profile of the source, respectively.

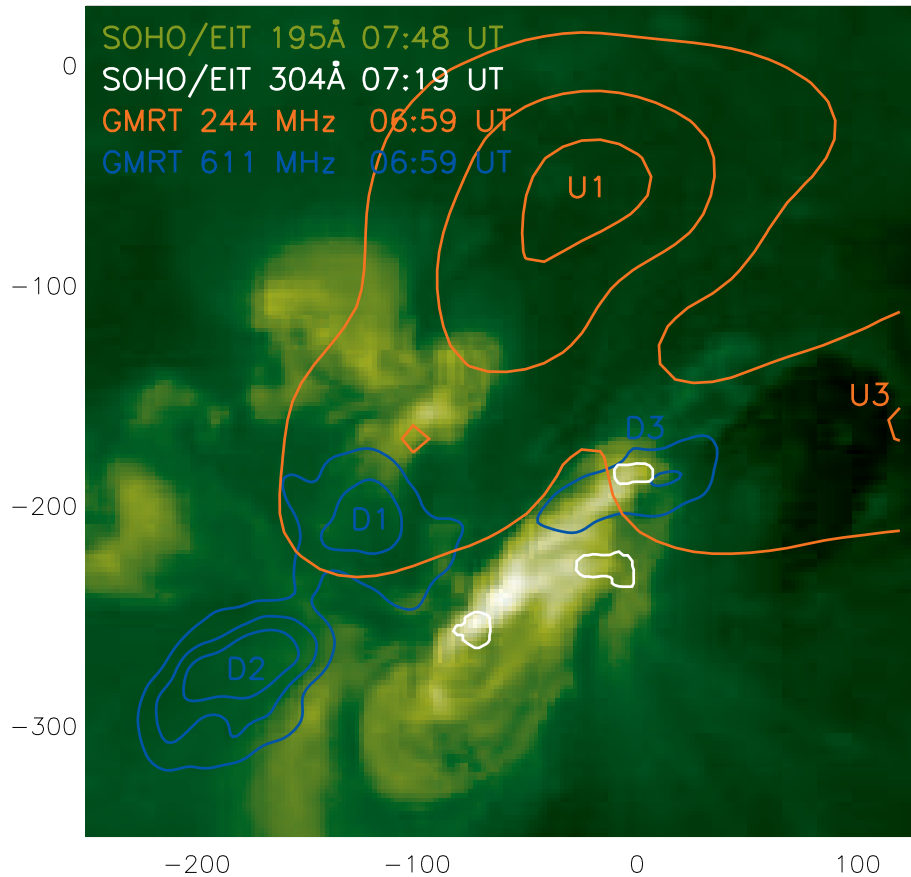


**Figure 5.** Superposition of the radio sources (same as in Figure 4) on top of the SoHO/EIT 195 Å observations taken at 7:48 UT. The EIT 195 Å observations are saturated to  $2 \times 10^3$   $\text{DN s}^{-1} \text{px}^{-1}$  and shown in logarithmic intensity scale for better visibility of fainter emitting loop systems. The flare arcade footpoints observed using the filter 304 Å at 07:19 UT are shown as white contours corresponding to  $10^3$   $\text{DN s}^{-1} \text{px}^{-1}$ .

The cross-correlation coefficients between pairs of all GMRT U and D sources show that there is only one pair with correlation higher than 75%. This pair is the sources U1 and D1 with the cross-correlation coefficient of 81%. This degree of correlation indicates that these radio sources can have a common origin.

The maximum of the cross-correlation coefficient is flat if the time lag of U1 with respect to D1 ranges 0–50 s. It indicates that first parts of radio fluxes D1 and U1 are correlated by some fast moving agents (possibly beams) and the second parts by slowly moving agents (possibly waves).

## 2.2. Photospheric magnetic field and the EUV flare

The GMRT interferometric observations offer the advantage of direct spatial comparison with the photospheric magnetic field and the EUV flare morphology, as observed by the SoHO/MDI and SoHO/EIT instruments, respectively. The



**Table 2.** Basic parameters derived for radio bursts at GMRT frequencies.

Frequency [MHz]	Source	Fundamental frequency altitude [Mm]	Plasma density [cm <sup>-3</sup> ]	First harmonic altitude [Mm]
244	U1–U3	48	$7.4 \times 10^8$	86
611	D1–D3	22	$4.6 \times 10^9$	40

comparison of the radio sources loci with the MDI magnetogram is presented in Figure 4. The magnetogram was observed at 06:24 UT and rotated to the time 06:59 corresponding to the radio observations using the SolarSoftware routine *drot\_map.pro*. The time of the radio observations, 06:59 UT, is chosen because it corresponds to the times of the first radio peaks in the sources U1 and D1.

The radio sources are located in a quadrupolar magnetic configuration consisting of two active regions, NOAA 10824 and 10825 (Figure 4). Both active regions are bipolar with a  $\beta$ -configuration. The AR 10824 is located approximately at the heliographic latitude of  $\approx -13^\circ$  and contains a well-developed, leading negative-polarity sunspot. Other polarities consist of plage regions or pores, which is the case also for the AR 10825 located at latitudes of  $\approx -7^\circ$ . A notable feature is that the radio sources are *not* located on top of the main magnetic polarities, but, in general, they overlie weak-field regions.

The SoHO/EIT instrument was performing full-disc observations in the 195 Å filter with a cadence of approximately 12 minutes. Observations in other filters, *i.e.* 171, 284 and 304 Å were performed at 07:00, 07:06 and 07:19 UT, respectively. Due to poor pointing information of the EIT instrument, the EIT 304 Å observations were coaligned manually with the MDI observations by matching the EIT 304 Å brightenings with small magnetic polarities observed by MDI, which show good spatial correlation (Ravindra and Venkatakrishnan, 2003). We estimate the error of this manual coalignment to be  $\approx 5$  arcsec.

In the EIT 304 Å observations, three flare arcade footpoints are discernible, shown in Figure 5 as white contours corresponding to the observed intensity of  $10^3$  DN s<sup>-1</sup> px<sup>-1</sup>. All three footpoints are located well within the AR 10824, with one of them in the positive polarity and the other two in the negative polarities North of the sunspot. EIT 195 Å observations show cooling system of flare loops connecting these three footpoints. The flare loops are well-visible at 195 Å at 07:48 UT and are shown in Figure 5. The global magnetic configuration of AR 10824 is that of a sigmoid with large shear. The magnetic configuration of the neighboring AR 10825 is near-potential.

Comparison of the loci of the radio sources with the EUV flare morphology (Figure 5) shows that the radio sources have no direct spatial correspondence with the EUV flare loops or their footpoints. The source D3 is an exception, since it overlies a portion of the flare loops. The sources U1, U3, D1 and D2 are located in the area of weak EUV emission.

### 3. Magnetic structure of active regions NOAA 10824 and 10825

#### 3.1. Magnetic field extrapolation and the altitude of the radio emission

To investigate the relationship between the radio sources and the structure of the magnetic field of active regions NOAA 10824 and 10825, we performed an extrapolation of the SoHO/MDI magnetogram (Figure 4) observed at 06:24 UT prior to the flare and associated radio events. The extrapolation was carried out in linear force-free approximation, where the magnetic field  $\vec{B}$  given by the solution of the equation

$$\vec{\nabla} \times \vec{B} = \alpha \vec{B}, \quad (1)$$

for  $\alpha = \text{const.}$  The solution is subject to the boundary condition  $B_z(x, y, z = 0)$  given by the observed magnetogram, where  $0 < x < L_x$  and  $0 < y < L_y$ . The constant  $\alpha$  is subject to the condition  $\alpha < \alpha_{\text{max}} = 2\pi/\max(L_x, L_y)$ , otherwise the magnetic field is non-physical. We utilized the Fourier transform method developed by Alissandrakis (1981) and Gary (1989). This method allows for extrapolation of the part of the observed magnetogram in a cartesian geometry. The computational box is shown in Figures 6 and 7.

We calculated a range of linear force-free models with various values of  $\alpha$ . However, the flare loops are poorly approximated with  $\alpha = \text{const.}$ , even with large values of  $\alpha$  close to  $\alpha_{\text{max}}$ . The reason for this probably is the presence of differential shear within the active region (Schmieder *et al.*, 1996). Moreover, using large values of  $\alpha$  leads to poor fit to the observed shape of the coronal loops in the AR 10825, which is close to the potential state ( $\alpha = 0$ ). Therefore, we chose to extrapolate in the potential approximation. We also note that the potential approximation does usually a good job in capturing the topological structure of the active region (though not at sigmoid locations, *e.g.* Schmieder and Aulanier 2003).

To compare the 3D magnetic field geometry with the loci of the radio sources, observed in a 2D plane of the sky, the approximate altitude at which the radio emission originates must be determined. To do that, we consider the parameters of the radio bursts (at GMRT frequencies) and the solar atmosphere density model (Aschwanden, 2002) for the radio plasma emission at fundamental frequency and the first harmonic (see also Section 3.2). We use Aschwanden's density model because it was derived from radio observations. The basic parameters of the radio sources are derived and summarized in Table 2 where the plasma density values belong to the fundamental frequency altitude.

#### 3.2. Magnetic topology and its relation to radio sources

The extrapolated magnetic field contains a pair of coronal magnetic null points between the two active regions. The negative and positive coronal null points are denoted by red (SE) and blue (NW) arrows in Figure 6. On this figure, the dark-red and dark-blue contours correspond to positive and negative photospheric polarities, respectively, with  $B_z = \pm 50$  and 500 G. Since the magnetic field of AR 10825 is weaker, the null points are located closer to this active region than

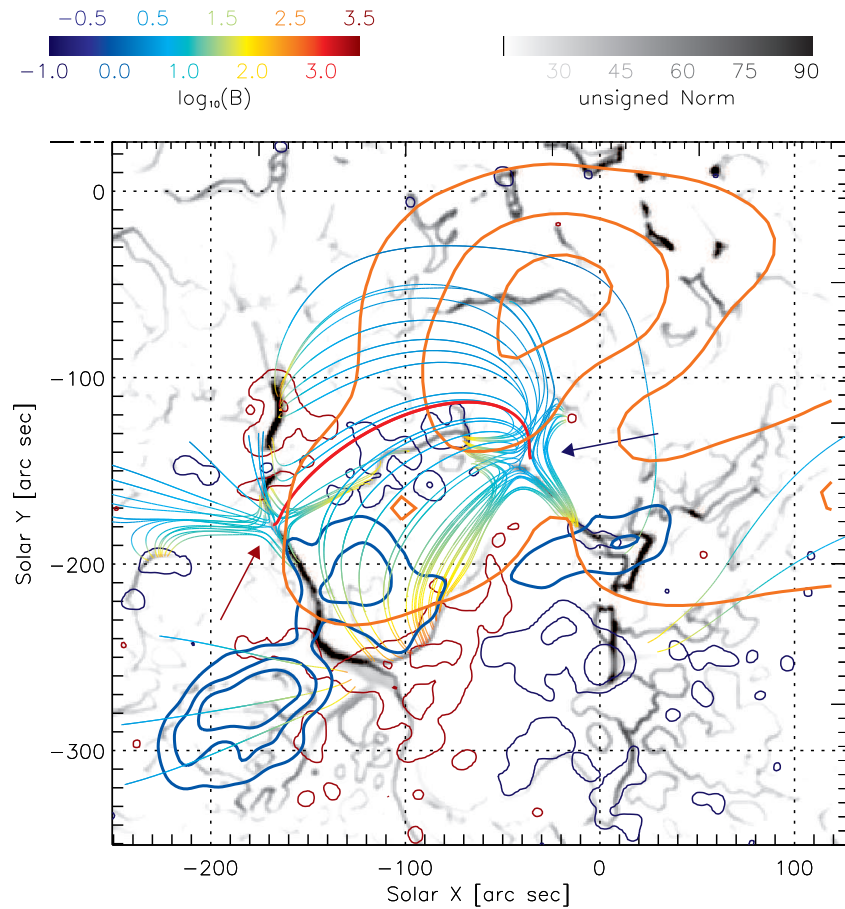


**Figure 6.** Plane-of-the-sky projection of the extrapolated magnetic field. Red (SE) and blue (NW) arrows show the locations of the positive and negative coronal magnetic null points, respectively. The separator lying at the intersection of the respective fans is plotted as thick red line. The magnetic field lines are colored according to the local magnetic field, in the range of  $\log_{10}(B/T) \in (-1.0, 3.5)$ . The thin, dark-red and dark-blue contours denote positive and negative photospheric polarities, respectively. The two contour levels correspond to  $B_z(z=0) = \pm 50$  and 500 G. Shades of gray show the photospheric intersections of the quasi-separatrix layers. The contours of the GMRT sources are located at the altitudes corresponding to the fundamental frequency (Table 2) and are shown as thick orange (U1-3) and blue (D1-3) contours, respectively.

to the larger AR 10824. The existence of these null points is a consequence of the multipolar structure of the magnetic field (*e.g.* Longcope 2005 and references therein). The magnetic structure in the vicinity of these null points is shown using several field lines regularly distributed near the null points. The fan surfaces of these null points intersect, forming a separator (Baum and Bratenahl, 1980; Longcope, 2005). The separator is found manually by trial-and-error and is shown by a thick red line.

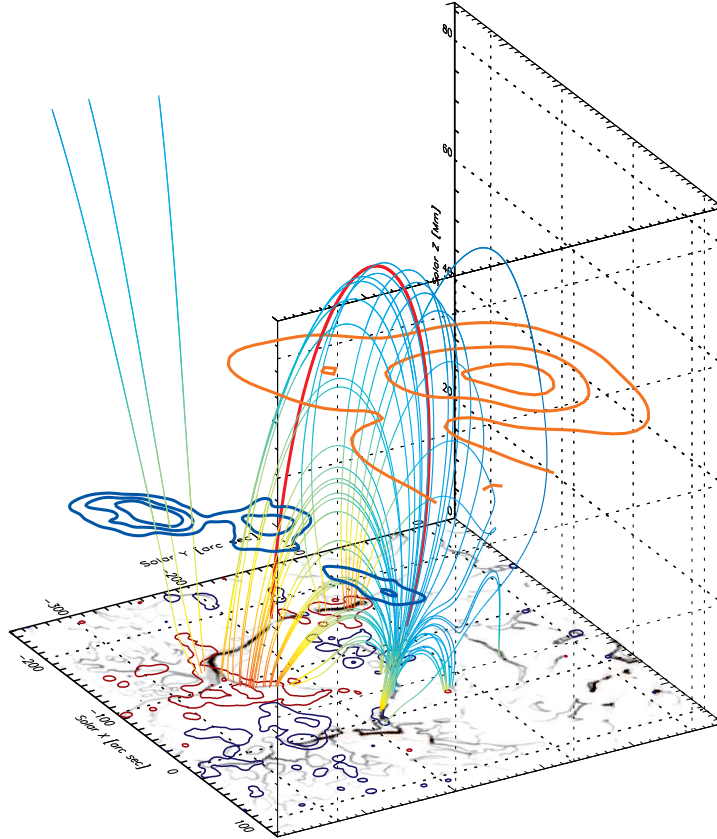


**Figure 7.** Same as in Figure 6, but in a 3D projection to show the altitudes of the individual field lines as well as individual radio sources. Only the field lines lying in the vicinity of the negative null point or passing through the source D2 are shown for clarity.

Both the spine and the fan surface of the negative null point are closed within the computational domain, while the fan surface of the positive null point is open. This is not typical of coronal null points (Pariat, Antiochos, and DeVore, 2009; Del Zanna *et al.*, 2011). Both fan surfaces form a part of the quasi-separatrix layers (Priest and Démoulin, 1995; Démoulin *et al.*, 1996; Démoulin *et al.*, 1997) as

$$N(x, y) = \left( \left( \frac{dX}{dx} \right)^2 + \left( \frac{dX}{dy} \right)^2 + \left( \frac{dY}{dx} \right)^2 + \left( \frac{dY}{dy} \right)^2 \right)^{1/2}, \quad (2)$$

where the starting footpoint of a field line at  $z = 0$  is denoted as  $(x, y)$  and its opposite footpoint as  $(X, Y)$ . The unsigned norm is computed irrespective of the direction of the footpoint mapping. We note that the correct definition of quasi-separatrix layers is through the squashing factor  $Q$  or the expansion-contraction factor  $K$  (Titov, Hornig, and Démoulin, 2002), which are invariants with respect to the footpoint mapping direction. Here, we use the unsigned norm, since it is much less sensitive to the errors arising because of the measurement noise and numerical derivation due to finite magnetogram resolution, and at the same time gives a good indication of the expansion-contraction factor  $K$ .

The sources U and D are plotted as thick blue and thick orange contours, respectively. These sources are plotted in height corresponding to the altitudes given by the fundamental frequencies (Table 2). It is clearly seen that both U1 and D1 are lying along the fan of the negative null point, with the field lines passing through the D1 being separated by the separator (Figures 6 and 7). Therefore, both the U1 and D1 lie along a common magnetic structure, providing straightforward explanation for the observed correlation between these two sources (Section 2.1). The separator also passes through U1, as does some other fan field lines rooted in AR 10825.

We note that the fan of the negative null-point covers only a part of the source U1. The rest of the U1 is associated with closed field lines rooted in the positive polarity of the AR 10825, in direct vicinity of the footpoints of the fan field lines. One example of such field lines is plotted in Figures 6 and 7. That there are structures other than the fan of the negative null-point passing through the source U1 offers explanation for the fact that the correlation coefficient between U1 and D1 is smaller than one.

The sources D2 and U3 are located on the field lines that are open within the computational box. The footpoints of these field lines are located in the AR 10824 in the vicinity of the photospheric quasi-separatrices with highest  $N$  separating the open and closed magnetic flux (Figure 6). Overall, we conclude that the field lines passing through the sources D1, D2, U1 and U3 are rooted in the vicinity of the flare arcade footpoints (compare Figures 5 and 6), while the source D3 appears to be connected directly to flare loops. These observations point out the fact that even a localized, weak flare can cause a widespread perturbation involving a large portion of the surrounding magnetic field and its topological features.

We stress that the goodness of the match between the extrapolated magnetic field and the radio sources is subject to the approximations used. *E.g.* presence of electric current in the model of the magnetic field would alter the geometry of the magnetic field. In particular, using a linear force-free approximation would mostly affect the longest field lines passing through the source U1. Additionally, the density model of (Aschwanden, 2002) provides only a single altitude for the emission of each radio frequency, while in reality the density profile and thus the altitude of emission can be different for each field line. However, the available longitudinal MDI magnetogram and the EIT data do not provide necessary constraints (Section 2) for using more elaborate models of the magnetic field or density throughout the observed radio-emitting atmosphere.

**Table 3.** Characteristics periods  $P$  for wavelet power spectra showing a tadpole pattern.

Source	Frequency [MHz]	Period $P$ [s]
U1	244	83, 25, 22, 11, 10
D1	611	76, 22, 13

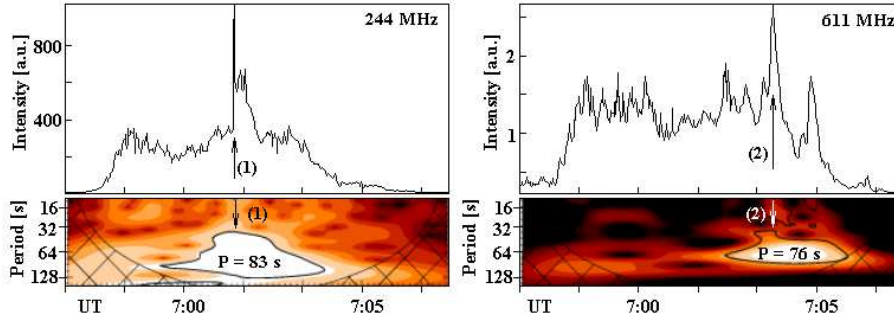


**Figure 8.** Examples of the wavelet power spectra showing tadpole patterns with characteristics periods  $P$  (bottom panels) in comparison with the GMRT radio fluxes (upper panels) at 244 MHz (source U1) and 611 MHz (source D1) frequencies. The lighter area shows a greater power in the power spectrum and it is bound by the solid contour of the confidence level  $>95\%$ . The hatched regions belong to the cone of influence with edge effects due to finite-length time series. The arrows (1) and (2) correspond to 7:01:30 and 7:03:52 UT, respectively.

We also note that the magnetic connectivity between U1 and D1 exists only if these sources are assumed to emit at the fundamental frequency (Table 2). If the origin of the radio emission would be the second harmonic, the radio emission should occur at altitudes which are higher than the vertical extent of the negative null point fan. This point is discussed further in Section 5.

#### 4. Wavelet analysis of the GMRT time series

To investigate the nature of the disturbance giving rise to the radio sources, an analysis of possible periodicity of radio time series at all frequencies, detected by the GMRT instrument, was made using the Morlet wavelet transform method (Torrence and Compo, 1998). We focused on the well correlated GMRT sources U1 and D1.

The wavelet power spectra at all frequencies of the GMRT instrument show the tadpole patterns (Nakariakov *et al.*, 2004) with characteristics periods  $P$  (Mészárosová *et al.*, 2009a, 2009b) in the range 10–83 s.

These periods were detected in the entire studied time interval 06:50–07:12 UT and are listed in Table 3. The periods of about 10 s were found at all frequencies.

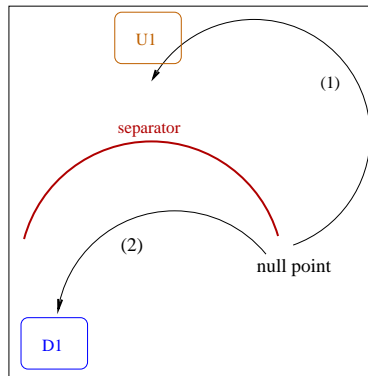


**Figure 9.** Scheme of the suggested scenario for the well-correlated sources U1 and D1 lying along the fan of the coronal null point. Magnetoacoustic waves move along magnetic field lines (trajectories (1) and (2)). The separator is located between these trajectories.

Figure 8 shows two examples of the wavelet power spectra of the well correlated radio sources U1 and D1 showing tadpole patterns (bottom panels) with the longest characteristic periods  $P$  listed in Table 3. In this figure, the arrows (1) and (2) are used to denote the times of 7:01:30 and 7:03:52 UT, respectively. These times correspond to the main peaks of the flux shown in the upper panels and the occurring tadpole head maximum shown in bottom panels. It has been proposed that the tadpoles indicate arrival of the magnetoacoustic wave trains at the radio source (Nakariakov *et al.*, 2004; Mészárosová *et al.*, 2009a, 2009b).

Although the U1 and D1 radio fluxes are well correlated (81%) the sources U1 and D1 are not the same in all details. Different appearance of the tadpoles in Figure 8 reflects different plasma parameters in the sources U1 and D1 (Jelínek and Karlický, 2012). This is expected, since these tadpoles have different characteristic period  $P$ , which means that they are propagating in different waveguides (see Section 5).

## 5. Discussion and Conclusions

We studied solar interferometric maps (Figures 1 and 2) and time series of the six individual radio sources, U1–U3 at 244 MHz and D1–D3 at 611 MHz (Figure 3), observed by the GMRT instrument with 1 s time resolution during the B8.9 flare on 26 November 2005. We determined that only sources U1 and D1 are well correlated with the cross-correlation coefficient of 81%.

Generally, the positions of the radio sources can be influenced by refractive effects. They play a role in the solar atmosphere as well as in the Earth ionosphere. As concerns to the effects in the solar atmosphere, our low frequency 244 MHz source U1 (which is the main feature under study together with the source D1) is nearly in the disk center, see Figure 1 or 4. In the disk center the refractive effects come to zero. Similarly, the D1 source at 611 MHz is close to

the disk center. We note that the phase calibration process at GMRT corrects the ionospheric refraction.

Comparison of the GMRT interferometric maps with the EUV observations of the flare by the SoHO/EIT instrument showed that only the source D3 can be connected to the system of flare loops. All other radio sources are located well away from the X-ray and EUV flare (*cf.* Benz, Saint-Hilaire, and Vilmer 2002). Potential extrapolation of the observed SoHO/MDI magnetogram in combination with the solar coronal density model of Aschwanden (2002) allowed us to find the connection of these other radio sources to the magnetic field of the observed active regions and their magnetic topology. The sources U1 and D1 were found to lie along the fan of a negative coronal null point. That the sources U1 and D1 lie along a common magnetic structure offers explanation for their observed correlation. The sources D2 and U3 lie at open field lines anchored near the quasi-separatrices in the vicinity of the flare arcade footpoints.

The connection between the radio sources and the magnetic field, as found in Section 3.2 is valid only if the radio emission originates at the fundamental frequency. This is because the altitudes corresponding to the first harmonic are too high (Table 2). We note that the emission at the first harmonic is usually considered to be stronger than at the fundamental frequency, due to the strong absorption for the fundamental emission. However, there are cases (*e.g.* enhanced plasma turbulence in the radio sources) which reduces this absorption and thus the emission at the fundamental frequency can be stronger than at the first harmonic.

Based on the results above, we conclude that even the observed localized flare is able to cause a widespread perturbation involving a large portion of the topological structure of the two active regions. This perturbation can be understood in the following terms: As the flare progresses, the flare arcade footpoints move away from each other. Since these footpoints correspond to the intersections of the quasi-separatrix layers with the photosphere (Démoulin *et al.*, 1996; Démoulin *et al.*, 1997), the increase of their distance perturbs the surrounding magnetic field and excite waves. If the surrounding, perturbed magnetic field contains null points, these can collapse and form a current sheet, thereby commencing reconnection in regions not directly involved in the original flare. This can then be also the mechanism for sympathetic flares and eruptions (Moon *et al.*, 2002; Khan and Aurass, 2006; Jiang *et al.*, 2008; Török *et al.*, 2011; Shen, Liu, and Su, 2012).

For the first time, wavelet tadpole patterns with the characteristic periods of 10–83 s (Table 3) were found at metric radio frequencies. We have interpreted them in accordance with the works of Nakariakov *et al.* (2004) and Mészárosová *et al.* (2009a, 2009b) as signatures of the fast magnetoacoustic waves propagating from their initiation site to studied radio sources U1 and D1.

The mechanism for initiation of the inferred magnetoacoustic waves present in the radio sources can thus be both the observed EUV flare and the flare-induced collapse of the null point located in the surrounding magnetic field. These waves propagated towards radio sources along magnetic field lines. They arrived at the radio sources (see the wavelet tadpoles in Figure 8) and modulated the radio



emission there. We expect that the magnetoacoustic waves, through their density and magnetic field variations, modulate the growth rates of instabilities (like the bump-on-tail or loss-cone instabilities), which generate plasma- as well as the observed radio waves.

The schematic scenario for the well-correlated sources U1 and D1 lying along the fan of the coronal null point is shown in Figure 9. Magnetoacoustic wave trains move along magnetic field lines (trajectories 1 and 2). The separator is located between these trajectories (*i.e.* between two groups of magnetic field lines (*cf.* Figure 6)). The distances between the null point and radio sources along the magnetic field lines are obtained directly from the extrapolation and allow the determination of the velocities of the magnetoacoustic waves. The averaged distances between the radio source and the null point, are about 53 and 103 Mm for the U1 and D1, respectively. We considered the time intervals  $t_2 - t_1$  and  $t_3 - t_1$  where  $t_1$  is the time of triggering of the magnetoacoustic wave trains. We assume that these trains propagating to the source U1 as well as to the source D1 were generated simultaneously at the beginning of the radio event, *i.e.* at the start time of U1 and D1 sources (Table 1). The times  $t_2$  and  $t_3$  correspond to the times of tadpole head maxima (arrows (1) and (2), Figure 8), respectively. Thus, the mean velocities of the magnetoacoustic waves are 260 and 300 km s<sup>-1</sup> for U1 and D1 sources, respectively.

Now, let us compare these mean velocities with the Alfvén velocities at the radio sources at U1 and D1. Taking plasma densities from Table 2 and the magnetic field from the extrapolation ( $B = 3$  G at U1 and 13 G at D1) the Alfvén velocity at these sources are  $v_A = 220$  and 390 km s<sup>-1</sup>, respectively. These velocities are in agreement with previous results, considering that the Alfvén velocities change along the trajectory of these magnetoacoustic waves, starting from the coronal null point.

Thus, knowing the Alfvén velocities in the radio sources, we can estimate also the width  $w$  of the structure through which the magnetoacoustic wave trains are guided. Namely, the period of this magnetoacoustic wave can be estimated as  $P \simeq w/v_A$  (Nakariakov *et al.*, 2004). Thus, the widths  $w$  of the structures guiding the magnetoacoustic waves (modulating the radio emission) are 18 Mm ( $83 \text{ s} \times 220 \text{ km s}^{-1}$ ) and 30 Mm ( $76 \text{ s} \times 390 \text{ km s}^{-1}$ ) in the U1 and D1 radio sources, respectively. This rough estimation confirms that the extent of the structure guiding magnetoacoustic waves is within the width of the fan of magnetic field lines in both radio sources. The wavelet tadpoles with shorter periods (Table 3) show that within the large structure guiding long period magnetoacoustic wave trains ( $P \sim 80$  s), there are also narrower waveguides guiding shorter period waves.

The complex of radio sources U1–U3 and D1–D3 includes the whole topological structure of the active area contrary to the rather localized EUV sources (Figure 5). This is in line with the observed radio sources being usually larger than the real sources due to scattering of radio waves (*e.g.* Benz, Battaglia, and Vilmer, 2011).

Considering the above presented estimations we can conclude that they support the scenario (Figure 9) of magnetoacoustic waves (wavelet tadpoles) in a fan structure above the coronal magnetic null point.

**Acknowledgements** We are thankful to Dr. E. Dzifčáková for encouraging discussions. H. M. thanks Dr. J. Rybák for his help with the wavelet analysis that was performed using the software based on tools provided by C. Torrence and G. P. Compo at <http://paos.colorado.edu/research/wavelets>. H. M. acknowledges support from the PCI/INPE Grant 33/2011 of the National Space Research Institute in Brazil. H. M. and M. K. acknowledge support from the Grant GACR P209/12/0103, the research project RVO:67985815 of the Astronomical Institute AS and the Marie Curie PIRSES-GA-2011-295272 RadioSun project. J. D. and M. K. acknowledge support from the bilateral project No. SK-CZ-11-0153. J. D. also acknowledges the support from the Scientific Grant Agency, VEGA, Slovakia, Grant No. 1/0240/11, Grant No. P209/12/1652 of the Grant Agency of the Czech Republic, Collaborative grant SK-CZ-0153-11 and Comenius University Grant UK/11/2012. We also thank the staff of the GMRT who have made these observations possible as well as the SoHO/MDI and SoHO/EIT consortia for their data. GMRT is run by the National Centre for Radio Astrophysics of the Tata Institute of Fundamental Research.

## References

- Afanasyev, A.N., Uralov, A.M.: 2012, *Solar Phys.* **280**, 561.  
 Alissandrakis, C.E.: 1981, *Astron. Astrophys.* **100**, 197.  
 Ananthakrishnan, S., Rao, A.P.: 2002, In: R. K. Manchanda and B. G. Pau (ed.) *Multi color universe*, Ebenezer Printing House, Mumbai **483**, 233.  
 Aschwanden, M.J.: 2002, *Space Sci. Rev.* **101**, pp. 187-189.  
 Aschwanden, M.J.: 2005, *Physics of the Solar Corona. An Introduction with Problems and Solutions (2nd edition)*.  
 Aurass, H., Rausche, G., Mann, G.: 2007, *Astron. Astrophys.* **471**, L37.  
 Aurass, H., Mann, G., Zlobec, P., Karlický, M.: 2011, *Astrophys. J.* **730**, 57.  
 Baum, P.J., Bratenahl, A.: 1980, *Solar Phys.* **67**, 245.  
 Benz, A.O., Saint-Hilaire, P., Vilmer, N.: 2002, *Astron. Astrophys.* **383**, 678.  
 Benz, A.O., Battaglia, M., Vilmer, N.: 2011, *Solar Phys.* **273**, 363.  
 Chen, B., Bastian, T.S., Gary, D.E., Jing, J.: 2011, *Astrophys. J.* **736**, 64.  
 De Moortel, I., Ireland, J., Walsh, R.W.: 2000, *Astron. Astrophys.* **355**, 23.  
 De Moortel, I.: 2009, *Space Sci. Rev.* **149**, 65.  
 Del Zanna, G., Aulanier, G., Klein, K.-L., Török, T.: 2011, *Astron. Astrophys.* **526**, A137.  
 Delaboudinière, J.-P., Artzner, G.E., Brunaud, J., Gabriel, A.H., Hochedez, J.F., Millier, F., et al.: 1995, *Solar Phys.* **162**, 291.  
 Démoulin, P., Hénoux, J.C., Priest, E.R., Mandrini, C.H.: 1996, *Astron. Astrophys.* **308**, 643.  
 Démoulin, P., Bagala, L.G., Mandrini, C.H., Hénoux, J.C., Rovira, M.G.: 1997, *Astron. Astrophys.* **325**, 305.  
 Domingo, V., Fleck, B., Poland, A.I.: 1995, *Solar Phys.* **162**, 1.  
 Gary, G.A.: 1989, *Astrophys. J. Suppl. Ser.* **69**, 323.  
 Harrison, R.A., Hood, A.W., Pike, C.D.: 2002, *Astron. Astrophys.* **392**, 319.  
 Jelínek, P., Karlický, M.: 2009, *European Physical Journal D* **54**, 305.  
 Jelínek, P., Karlický, M.: 2010, *IEEE Transactions on Plasma Science* **38**, 2243.  
 Jelínek, P., Karlický, M.: 2012, *Astron. Astrophys.* **537**, A46.  
 Jiang, Y., Shen, Y., Yi, B., Yang, J., Wang, J.: 2008, *Astrophys. J.* **677**, 699.  
 Karlický, M., Jelínek, P., Mészárosóvá, H.: 2011, *Astron. Astrophys.* **529**, A96.  
 Katsiyannis, A.C., Williams, D.R., McAteer, R.T.J., Gallagher, P.T., Keenan, F.P., Murtagh, F.: 2003, *Astron. Astrophys.* **406**, 709.  
 Kerdraon, A., Delouis, J.-M.: 1997, In: G. Trottet (ed.) *Coronal Physics from Radio and Space Observations, Lecture Notes in Physics, Berlin Springer Verlag* **483**, 192.  
 Khan, J.I., Aurass, H.: 2006, *Astron. Astrophys.* **457**, 319.  
 Kliem, B., Dammasch, I.E., Curdt, W., Wilhelm, K.: 2002, *Astrophys. J. Lett.* **568**, L61.

- Longcope, D.W.: 2005, *Living Reviews in Solar Physics* **2**, 7.
- Marsh, M.S., Walsh, R.W., Plunkett, S.: 2009, *Astrophys. J.* **697**, 1674.
- Marsh, M.S., De Moortel, I., Walsh, R.W.: 2011, *Astrophys. J.* **734**, 81.
- McLaughlin, J.A., Hood, A.W., De Moortel, I.: 2011, *Space Sci. Rev.* **158**, 205.
- Mercier, C., Subramanian, P., Kerdraon, A., Pick, M., Ananthakrishnan, S., Janardhan, P.: 2006, *Astron. Astrophys.* **447**, 1189.
- Mészárosová, H., Karlický, M., Rybák, J., Jiříčka, K.: 2009a, *Astrophys. J. Lett.* **697**, L108.
- Mészárosová, H., Karlický, M., Rybák, J., Jiříčka, K.: 2009b, *Astron. Astrophys.* **502**, L13.
- Mészárosová, H., Karlický, M., Rybák, J.: 2011, *Solar Phys.* **273**, 393.
- Moon, Y.-J., Choe, G.S., Park, Y.D., Wang, H., Gallagher, P.T., Chae, J., *et al.*: 2002, *Astrophys. J.* **574**, 434.
- Nakariakov, V.M., Arber, T.D., Ault, C.E., Katsiyannis, A.C., Williams, D.R., Keenan, F.P.: 2004, *Mon. Not. Roy. Astron. Soc.* **349**, 705.
- Ofman, L., Wang, T.J.: 2008, *Astron. Astrophys.* **482**, L9.
- Pariat, E., Antiochos, S.K., DeVore, C.R.: 2009, *Astrophys. J.* **691**, 61.
- Priest, E.R., Démoulin, P.: 1995, *J. Geophys. Res.* **1002**, 23443.
- Priest, E.R., Pontin, D.I.: 2009, *Physics of Plasmas* **16**(12), 122101.
- Ravindra, B., Venkatakrisnan, P.: 2003, *Solar Phys.* **214**, 267.
- Roberts, B., Edwin, P.M., Benz, A.O.: 1983, *Nature* **305**, 688.
- Roberts, B., Edwin, P.M., Benz, A.O.: 1984, *Astrophys. J.* **279**, 857.
- Scherrer, P.H., Bogart, R.S., Bush, R.I., Hoeksema, J.T., Kosovichev, A.G., Schou, J., *et al.*: 1995, *Solar Phys.* **162**, 129.
- Schmieder, B., Demoulin, P., Aulanier, G., Golub, L.: 1996, *Astrophys. J.* **467**, 881.
- Schmieder, B., Aulanier, G.: 2003, *Adv. Sp. Res.* **32**, 1875.
- Schwab, F.R.: 1984, *Astronom. J.* **89**, 1076.
- Shen, Y., Liu, Y., Su, J.: 2012, *Astrophys. J.* **750**, 12.
- Subramanian, P., White, S.M., Karlický, M., Sych, R., Sawant, H.S., Ananthakrishnan, S.: 2007, *Astron. Astrophys.* **468**, 1099.
- Swarup, G., Ananthakrishnan, S., Kapahi, V.K., Rao, A.P., Subrahmanya, C.R., Kulkarni, V.K.: 1991, *Current Science* **60**, 95.
- Titov, V.S., Hornig, G., Démoulin, P.: 2002, *Journal of Geophysical Research (Space Physics)* **107**, 1164.
- Tomczyk, S., McIntosh, S.W., Keil, S.L., Judge, P.G., Schad, T., Seeley, D.H., Edmondson, J.: 2007, *Science* **317**.
- Török, T., Panasenco, O., Titov, V.S., Mikić, Z., Reeves, K.K., Velli, M., *et al.*: 2011, *Astrophys. J. Lett.* **739**, L63.
- Torrence, C., Compo, G.P.: 1998, *Bulletin of the American Meteorological Society* **79**, 61.
- Trottet, G., Correia, E., Karlický, M., Aulanier, G., Yan, Y., Kaufmann, P.: 2006, *Solar Phys.* **236**, 75.
- Zuccarello, F., Contarino, L., Farnik, F., Karlický, M., Romano, P., Ugarte-Urra, I.: 2011, *Astron. Astrophys.* **533**, A100.

